Optics & Laser Technology 192 (2025) 113495

Contents lists available at ScienceDirect

Optics and Laser Technology

journal homepage: www.elsevier.com/locate/optlastec

In-situ monitoring and metallographic observations of mass transfer and defect formation during AlSi10Mg additive manufacturing using powder sheets☆

Pengfei Guo [a,b,*], Joerg Volpp [c,*], Himani Naesstroem [a], Silvia Marola [d], Wenyou Zhang [b], Johanne Mouzon [a], Riccardo Casati [d], Michael Gibbons [b], Rocco Lupoi [b], Alexander F.H. Kaplan [a]

[a] Department of Engineering Sciences and Mathematics, Luleå University of Technology, 97187 Luleå, Sweden
[b] Trinity College Dublin, The University of Dublin, Department of Mechanical, Manufacturing & Biomedical Engineering, Dublin, Ireland
[c] Department of Engineering Science, University West, 461 86 Trollhättan, Sweden
[d] Politecnico di Milano, Department of Mechanical Engineering, Via la G. La Masa 1, 20156 Milano, Italy

ARTICLE INFO

Keywords:
Laser directed energy deposition
Powder sheet
AlSi10Mg alloy
High-speed imaging
Mass transfer
Defect formation

ABSTRACT

Metal additive manufacturing using powder sheets (MAPS) melts powder attached in a sheet with a polymer binder, avoiding risks of loose powders in material waste, safety and health during laser additive manufacturing among other for e-mobility applications. However, this concept remains challenging for aluminum alloys due to occurring defects. To address this challenge, the mass transfer and defect formation mechanism during MAPS-AlSi10Mg were investigated using high-speed imaging and metallographic observations. The results showed that the mass transfer is realized via droplets formed first from the powder sheet in front of the melt pool and their incorporations into the melt pool. However, a much laser defocusing significantly inhibits the droplets' incorporation into the melt pool and promotes the balling. Polymer coatings or it wrapped into the AlSi10Mg droplets, generates the inclusions once the droplets were incorporated into the melt pool. Furthermore, under the laser beam in focus, the large particle-size powder sheet, powder side up or low scanning speed easily induce pores via shielding gas/polymer vapor inclusion. The laser defocusing of +15 mm, average laser intensity of 1.6×10^5 W/cm^2, and binder side up induce defect-free tracks, owing to the complete removal of polymers by their sufficient evaporation and powder agglomeration spatters. This work unveils that the droplets' incorporation into melt pool leads to the mass transfer of MAPS-AlSi10Mg while the droplets containing polymers and gas/vapor inclusion generate inclusions and pores. Meanwhile, the defect-free production strategy of suitable defocusing and high laser intensity is proposed.

1. Introduction

Modern electric vehicles, such as scooters, cars or even planes [1] use light-weight materials (e.g. aluminum alloys) for multiple parts and components. During usage those parts can wear [2] and need to be replaced. Smart repair solutions can increase the product lifetimes. Additive Manufacturing (AM) methods showed their capability to repair components (e.g. [3]). In particular for enabling efficient material usage for e-mobility applications, AM-based repair solutions are required.

Laser directed energy deposition of metals (DED-LB/M), one of the categories for laser additive manufacturing (LAM), can directly produce the components from their 3D models via point-by-point, line-by-line, and layer-by-layer deposition with the advantages of no mould, free design, high-performance manufacturing, and near-net-shape-production [4]. The metallic powdered material/wire is fed simultaneously with the movement of laser, and the material addition is realized by inserting the powder/wire into the melt pool formed in the substrate. Based on this technical feature, DED-LB/M has been extended from 3D printing to some specific fields, such as, high-deposition-rate manufacturing (adopting high laser power with large-size laser beams and high powder/wire feeding speeds) [5], re-manufacturing [6], repairing [7,8], and coating [9], which has promoted more extensive

☆ This article is part of a special issue entitled: 'LaserEMobility' published in Optics and Laser Technology.

* Corresponding authors.
E-mail addresses: guop@tcd.ie (P. Guo), jorg.volpp@hv.se (J. Volpp).

https://doi.org/10.1016/j.optlastec.2025.113495
Received 16 January 2025; Received in revised form 6 May 2025; Accepted 2 June 2025
Available online 9 July 2025

applications. It is consistent with the fact that the revenue share of DED-LB/M technologies is predicted to be increased from 8.3 % to 11.1 % by 2025 [10].

One of the most pertinent issues when using metallic powder feedstock, however, is that the current DED-LB/M systems often exhibit a small powder catchment efficiency of well below 50 % [11]. Usually, the undeposited powders are unavailable for being reused in the next DED-LB/M process due to the interactions of powders with the laser beam, and the atmosphere. These may induce contaminations of the powders including the modification of the composition and particle morphology, which is detrimental to the forming quality of the builds. The powder waste will not only cause serious economic, but present inferior environmental issues, which pose a challenge to the sustainability of DED-LB/M. In addition, some low-melting-point metal powders are highly flammable and combustible, which further increases the risks of health and safe issues during DED-LB/M, disposal, and transportation process.

Novelly, the metal additive manufacturing using powder sheet (MAPS) [12] has been proposed to avoid these issues mentioned above. The illustration of MAPS is presented in Fig. 1. It can be seen that a "powder sheet" delivery system replaces the loose powder delivering system based on the DED-LB/M equipment. Furthermore, high productivity and local material application for component repair is possible with minimum material loss.

The powder sheet is produced via solvent casting. The solution mixture of powders, polycaprolactone polymer, and chloroform ($CHCl_3$) are placed on a Teflon substrate firstly. Afterwards, the relative motion between the Teflon substrate and an immobilized 90° bevelled razor blade makes the solution mixture disperse uniformly on the Teflon substrate. After less than 15 min of drying, the powder sheet can be produced. The production process of the powder sheet and related set-up are introduced in details in Refs. [12,13]. Note that the side of the powder sheet closed to the Teflon substrate after production exhibits more surface polymer binder, thus it is named binder side and the opposite side is called powder side.

Until now, Prof. Lupoi and his workmates have conducted MAPS research around stainless steel. For instance, the effect of laser defocusing on manufacturing quality [14], process optimization using irregular-powder powder sheets [15], and relations of microstructure to mechanical properties [16] have been systematically investigated. Meanwhile, MAPS also has been successfully used in the forming of HEA CoNiCrFeMn [17] and multi-material (SS304-Inconel 718-SS304) [13]. These research have confirmed the feasibility of MAPS employing high scanning speed of larger than 60 m/min and small melt pool diameters of ~100 μm based on laser powder bed fusion process (PBF-LB/M, another method of LAM and based on preplacing powder in a powder bed [18]), and focused on developing the process-microstructure-property relations. However, as a novel raw material fed method, the mass transfer mechanism during MAPS is still not fully understood, especially when using a slow scanning speed (<5 m/min) and large melt pool diameter (>1 mm) widely used in DED-LB/M process.

Furthermore, previous research employed high-melting-point alloy powders (i.e., Fe-based and Ni-based alloys) in the powder sheets, which need more laser energy input during MAPS process and thus the evaporation of the polymers can be effectively promoted to induce less inclusion defects in the deposit. For the low-melting-point alloy powders (e.g., Al alloys), the separation of polymers from the melt pool is difficult and complex due to the small range between their respective boiling points, which easily leads to the generation of defects, such as inclusions or pores. In addition, large particle sizes within the powder sheets generate large spaces that contain more gas than small particle-size powder sheets, which is possibly to be brought into the melt pool to form pore defects. However, the defect formation mechanisms and their control is still lacking of in-depth investigation.

In the present work, the mass transfer mechanism during MAPS process is revealed for the first time. Meanwhile, the formation and control of defects during MAPS-AlSi10Mg process is systematically investigated. The paper is organized as follows. 1) The comparative investigations were conducted employing preplaced powder and powder sheets to reveal the difference of the melt pool dynamics. 2) The binder/powder side, particle size, defocusing, scanning speed, and average laser intensity were investigated to acquire the cross-section morphologies of the MAPS tracks and melt pool dynamics during MAPS-AlSi10Mg process. Their effects on mass transfer and melt pool dynamics were revealed. 3) The relationship between the main processing parameters, mass transfer and defect formation were developed. This work provides effective experimental dependence, and data supports to obtain defect-less AlSi10Mg tracks using MAPS method.

2. Experimental

2.1. MAPS system

The MAPS system, a modified DED-LB/M setup, was employed for the experiments (shown in Fig. 2). Note that the powder-feeding system was replaced by the preplaced powder sheet. The MAPS system is equipped with a 5 kW fiber laser with a wavelength 1070 ± 10 nm (IPG YRS-5000-S2T-Y16 Yb). The laser beam is inclined by 7° towards scanning direction to avoid laser optical reflection. The noble argon gas was supplied to the melt pool with a flow rate of 1.19 cm/s via a shielding nozzle with an inner diameter of 20 mm. The melt pool during

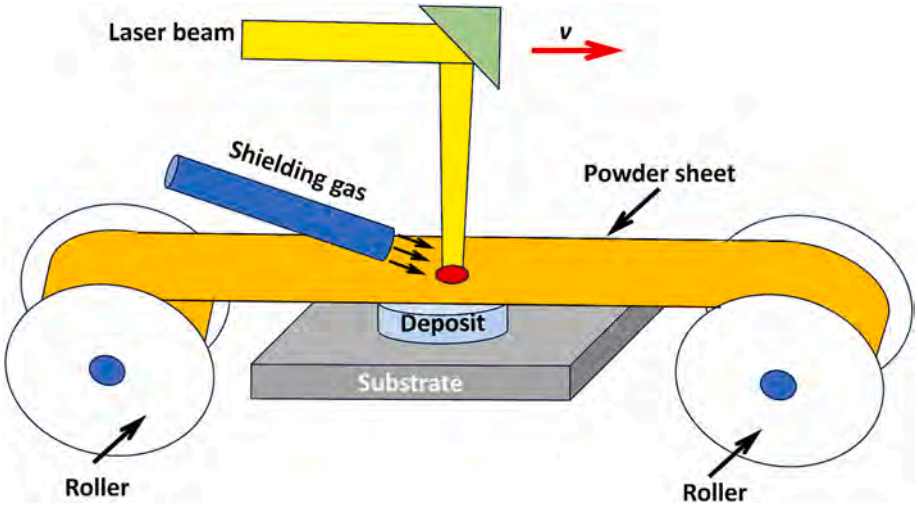

Fig. 1. Illustration of MAPS process.

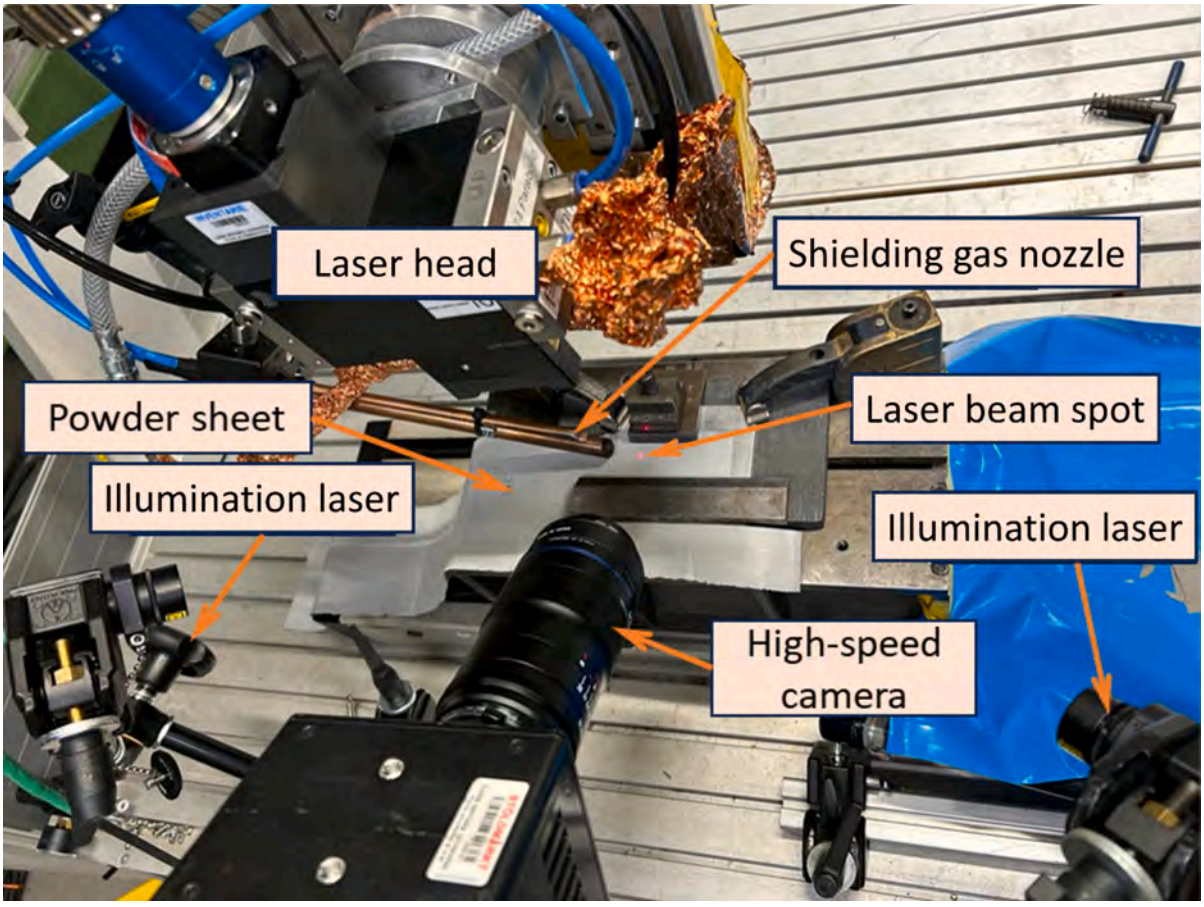

Fig. 2. MAPS system equipped with laser, worktable, powder sheet, shielding gas nozzle, high-speed camera and illumination system.

MAPS process was observed via a high-speed imaging (HSI), which was fixed perpendicularly at an angle of ~30°–75° from the horizontal plane to realize multiple-angle observations. Meanwhile, two sets of illuminations were installed around the HSI equipment to make the illuminations irradiate on the melt pool. For the comparative study, the preplaced powder method was also employed. The thickness of preplacing powder is fixed to 300 μm.

2.2. Feedstock material

Powders and powder sheets were employed as the feedstock material in the experiments, whose details are listed in Table 1. Note that preplaced powders were used for comparative study. For fully understanding the features of the powder sheets, the typical powder sheets with large and small powders (Type 1 and Type 2) were observed and characterized, as shown in Fig. 3. For Type 1 powder sheet, there are only powders visible without polymers on the powder side (shown in Fig. 3a) while some polymer binder is visible on the binder side (in Fig. 3b). Its thickness is about 287 μm and the polymers are filled between the powders, as presented in Fig. 3c. Similar to Type 1 powder sheet, Type 2 powder sheet also shows the powder side (Fig. 3d) and binder side (Fig. 3e). However, the particle size of Type 2 powder sheet is (60–200 μm), which is larger than that of Type 1 powder sheet (0–30 μm). From Fig. 3f, the thickness of Type 2 powder sheet is about 268 μm. The polymers partly filled the gap between powders and thus some interspaces full of gas survive. The commercial gas atomized powders were bought from CARPENTER ADDITIVE (20–63 μm) and IMR metal powder technologies GmbH (0–30 μm and 60–200 μm). The EN-AW

Table 1
Details of the powders and powder sheets employed in the experiments.

Feedstock	Powder size (μm)	Particle size distribution	Polymer-solvent solution (%)	Powder to polymer–solvent solution ratio	Average thickness (μm)
Powder (gas atomized powder from Deloro)	20–63	D_{10} = 24.8 μm D_{50} = 37.1 μm D_{90} = 57.7 μm	–	–	300
Type 0 powder sheet (gas atomized powder from CARPENTER ADDITIVE)	20–63	D_{10} = 24.8 μm D_{50} = 37.1 μm D_{90} = 57.7 μm	14	20 g/10 mL	207
Type 1 powder sheet (gas atomized powder from IMR metal powder technologies GmbH)	0–30	D_{10} = 6.6 μm D_{50} = 15.2 μm D_{90} = 24.0 μm	14	20 g/10 mL	287
Type 2 powder sheet (gas atomized powder from IMR metal powder technologies GmbH)	60–200	D_{10} = 42.6 μm D_{50} = 83.5 μm D_{90} = 157 μm	14	20 g/10 mL	268

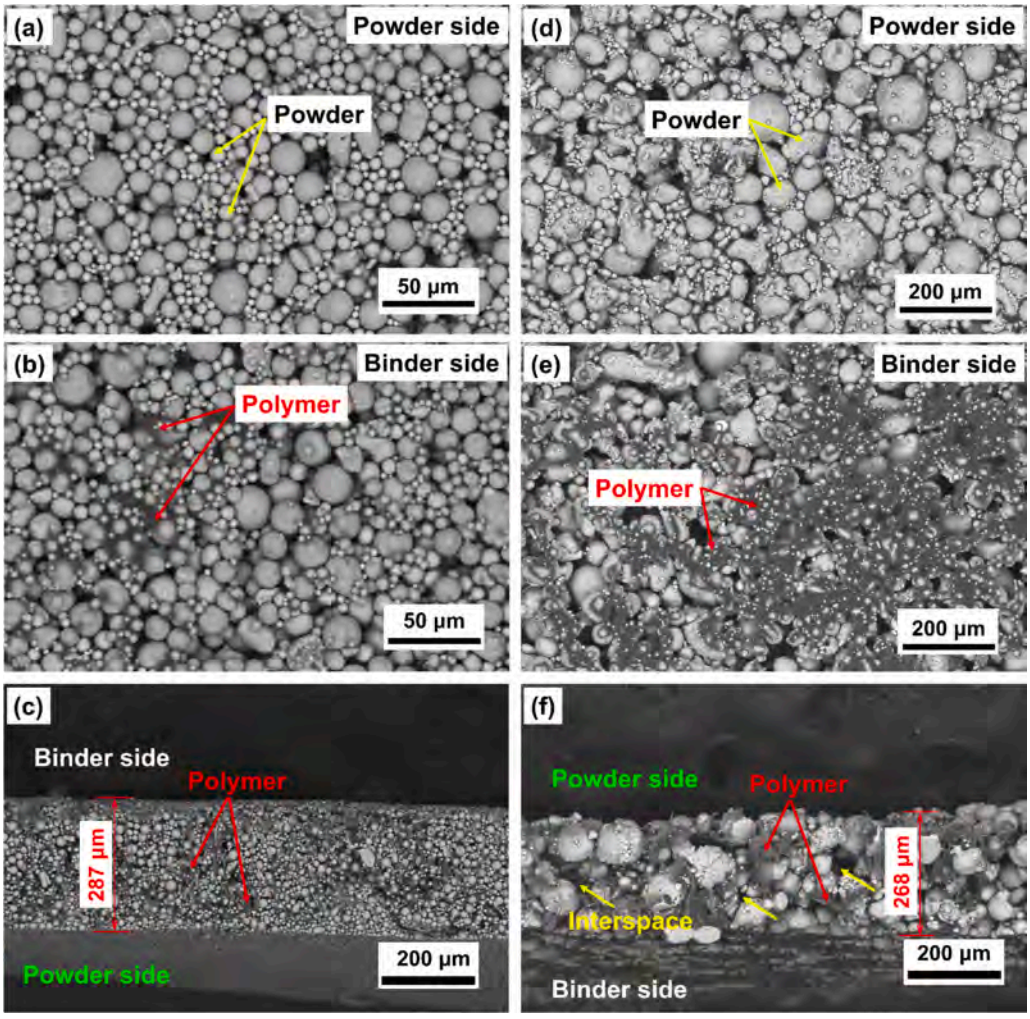

Fig. 3. Morphologies of the powder sheets. Surface morphologies of Type 1 powder sheet on (a) powder side, (b) binder side, and (c) the cross-section morphology. Surface morphologies of Type 2 powder sheet on (d) powder side, (e) binder side and (f) cross-section morphology.

6082 aluminum alloy substrate with a thickness of 3 mm was employed for all experiments.

2.3. Processing parameters

To comprehensively investigate the mass transfer and defect formation mechanisms during MAPS process, the powder sheet (type and upside), defocusing, laser power, and scanning speed were varied, as well as the average laser intensity (I, W/cm^2) under a specific defocusing. Note that I can be given as follows,

$$I = \frac{P}{A} = \frac{4P}{\pi D^2} \tag{1}$$

where laser power (P), beam area (A), and beam diameter (D) are

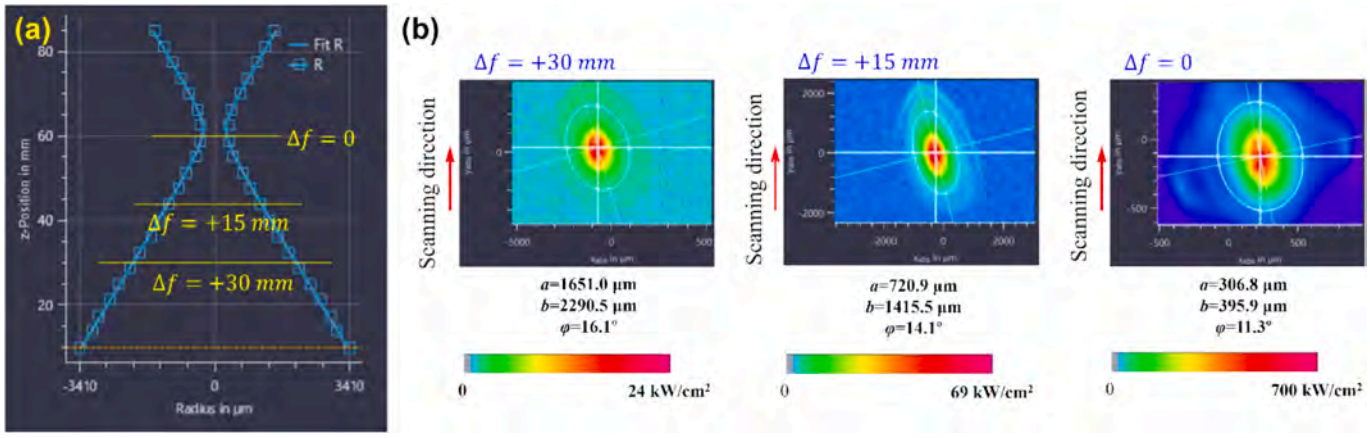

Fig. 4. (a) Illustrations of defocusing and (b) laser beam shape/energy distributions under different defocusing.

needed. From the equation, the average laser intensity presents the power per unit area.

Furthermore, the defocusing (Δf) of 0, +15, and +30 mm were employed during the MAPS experiments. The defocusing and the corresponding laser beam shape/energy distributions were measured under 500 W using FocusMonitor FM + device from PRIMES GmbH. The results are shown in Fig. 4a and b, respectively. Actually, $\Delta f = 0$ represents the focused laser, as exhibited in Fig. 4a. Fig. 4b shows that the laser beam presents ellipse, and the lengths of the long axis (a) and short axis (b) increase with the increasing positive defocusing. φ represents the angel between long axis and scanning direction. The detailed processing parameters employed in MAPS experiments are listed in Table 2.

Note that, 1–3 are adopted to comparatively study the effect of the preplaced powder and powder sheet on mass transfer and defect formation mechanisms. 1 & 2 and 4 & 5 are used to reveal the effect of binder side of the powder sheet; 1 & 4 are employed to investigate the effect of particle sizes; 3 & 7 are used to study the effect of defocusing; 1 & 3 and 4 & 6 are performed to investigate the effect of scanning speed; 8 & 9 are conducted to explore the effect of average laser intensity. Considering the laser power works accompanied closely with defocusing, the average laser intensity related to both of them is employed to reflect the effect of laser power.

2.4. Characterizations

The melt pool dynamics during MAPS-AlSi10Mg processes were recorded using HSI with a frame rate of 16,000 fps and shutter time of 10 μs. The cross section of MAPS-tracks were characterized using a Field Emission Scanning Electron Microscope (FE-SEM, Zeiss Sigma 500) from aspects of defects and the melt pool size (height, width and depth). Prior to observations, the samples were cut using an automatic precision cutting machine (Metkon Micracut 202). Afterwards, they were embedded in conductive resin, grinded using sand papers of #600, #1200 and #2500 in turn, and then polished by abrasive paste of 6, 3, and 1 μm. Note that the single cross-section on the middle part of the track with a stable and uniform surface morphology was taken from each track for correctly reflect the cross-section features.

Table 2
Parameters of the MAPS-AlSi10Mg experiments.

No.	Defocusing (Δf, mm)	Laser power (P, kW)	Scanning speed (v, m/min)	Powder sheet	Upside	Average laser intensity (I, W/cm^2)
1	+30	4.4	2	Powder	/	3.7×10^4
2	+30	4.4	2	Type 0	Binder side	3.7×10^4
3	+30	4.4	1.5	Type 1	Powder side	3.7×10^4
4	0	3	2.4	Type 1	Binder side	7.7×10^5
5	0	3	2.4	Type 1	Powder side	7.7×10^5
6	0	3	1.5	Type 1	Binder side	7.7×10^5
7	0	3	2.4	Type 2	Binder side	7.7×10^5
8	0	3	2.4	Type 2	Powder side	7.7×10^5
9	0	3	1.5	Type 2	Binder side	7.7×10^5
10	+30	3	1.5	Type 1	Binder side	2.5×10^4
11	+15	3.55	1.77	Type 1	Binder side	1.1×10^5
12	+15	5	2.5	Type 1	Binder side	1.6×10^5

2.5. In-situ monitoring

A high-speed camera named FASTCAM Mini UX100 was recording melt pool at a recording speed of 16,000 fps (except 10,000 fps for High-Speed Videos 1 and 2, and 5000 fps for High-Speed Video 5) with a frame size of 1280 × 312 pixels (except 1280 × 480 pixels for High-Speed Videos 1 and 2, and 1280 × 720 pixels for High-Speed Video 5), at a shutter time of 10 μs. Two illumination lasers with a maximum power of 50 W and a wavelength of 810 nm were employed to illuminate the melt pool. A band-pass filter of 810 nm was installed in front of the camera to block the scattered light of the processing laser with a wavelength of 1070 nm.

3. Results

3.1. Defect and melt pool dynamics using powder and powder sheet

Fig. 5 shows the cross-section morphologies of the laser powder-track produced with preplaced powder and MAPS-tracks using Type 1 powder sheet (corresponding to Experimental Nos. 1–3 with parameters of $\Delta f = +30$ mm and 4.4 kW). The track of the preplaced powder-track (Fig. 5a) shows no defects. However, when using powder sheets, inclusions and pores occur (Fig. 5b and c). Fig. 5b shows the cross-section morphology of the MAPS-track when the binder side is up while some inclusions and pores exist in the cross section. When the powder side is up and scanning speed is 1.5 m/min (Fig. 5c), there are even more inclusions with a smaller size in the cross section, as well as a larger pore. Obviously, the utilization of powder sheets induces the formation of defects, such as, inclusions and pores.

Fig. 6 shows the HSI frames of melt pool in Experiment Nos. 1–3 (corresponding to Fig. 5). Note that the ejections during the MAPS-AlSi10Mg process mainly contain solid spatter (i.e., un-melted powder flying away), powder agglomeration spatter (refers to liquid–liquid powder agglomeration), and metallic jet (i.e., liquid droplet ejected from the melt pool), according to the categories in Ref. [19].

Fig. 6a exhibits the HSI frame of the melt pool in Experiment No. 1 ($\Delta f = +30$ mm, 4.4 kW, 2 m/min, powder). In front of the melt pool, there is a melt pool lag. Within the melt pool lag area, the emerging droplet formed from the melting of the powders, which are incorporated into the approaching melt pool. There are no spatter and balling phenomena. The forming process is shown in the High-Speed Video 1 of the supplementary materials. Fig. 6b presents the HSI frame of the melt pool in Experiment No. 2 ($\Delta f = +30$ mm, 4.4 kW, 2 m/min, Type 1 powder sheet, and binder side up). It can be seen that the evaporation of polymers is intense. Some droplets are formed around the melt pool and there is some unevaporated polymer binder covered on the surfaces of the droplets. Only the droplets in front of the melt pool can be incorporated into the melt pool. Above the melt pool lag area, both the powder agglomeration spatter and solid spatter are occurring. These phenomena are presented in High-Speed Video 2 in the supplementary materials. Fig. 6c shows the HSI frame of the melt pool in Experiment No. 3 ($\Delta f = +30$ mm, 4.4 kW, 1.5 m/min, Type 1 powder sheet and powder side up). The intense evaporation of the polymer binder can be observed. In the melt pool lag area, the powder layer detaches from the powder sheet, moves towards the melt pool, and finally becomes droplets. Due to the laser recoil pressure, some small droplets become powder agglomeration spatter. Some droplets move along both sides of the melt pool to form balling. Others are captured by the melt pool. The process is shown in High-Speed Video 3 in the supplementary materials.

3.2. Defect and melt pool dynamics at different sheet orientations

Fig. 7 shows the cross-section morphologies of the MAPS-tracks using Type 1 powder sheet when binder or powder side was up (corresponding to Experimental Nos. 4–5 with parameters of $\Delta f = 0$ and 3 kW). Some inclusions, which wrapped in droplets, exist in the cross

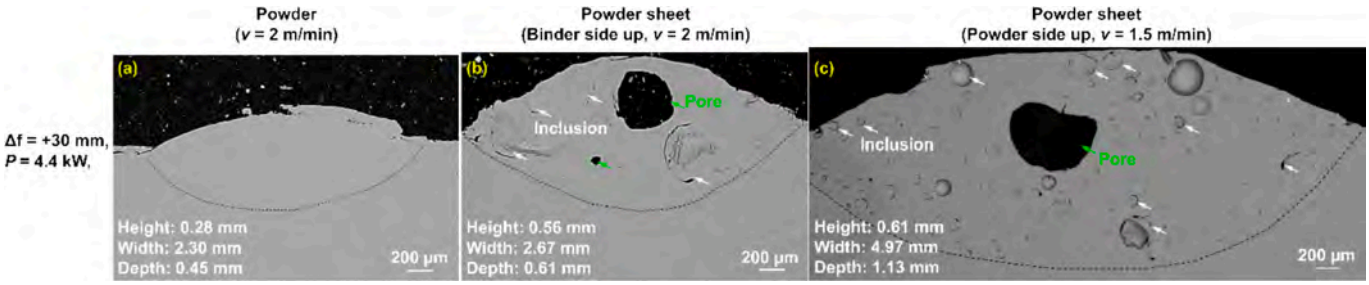

Fig. 5. Cross-section morphologies of the laser preplaced powder-tracks and MAPS-tracks using Type 1 powder sheet when binder or powder side is up. (a) Experiment No. 1 ($\Delta f = +30$ mm, 4.4 kW, 2 m/min, powder); (b) No. 2 ($\Delta f = +30$ mm, 4.4 kW, 2 m/min, Type 1 powder sheet, and binder side up); (c) No. 3 ($\Delta f = +30$ mm, 4.4 kW, 1.5 m/min, Type 1 powder sheet, and powder side up).

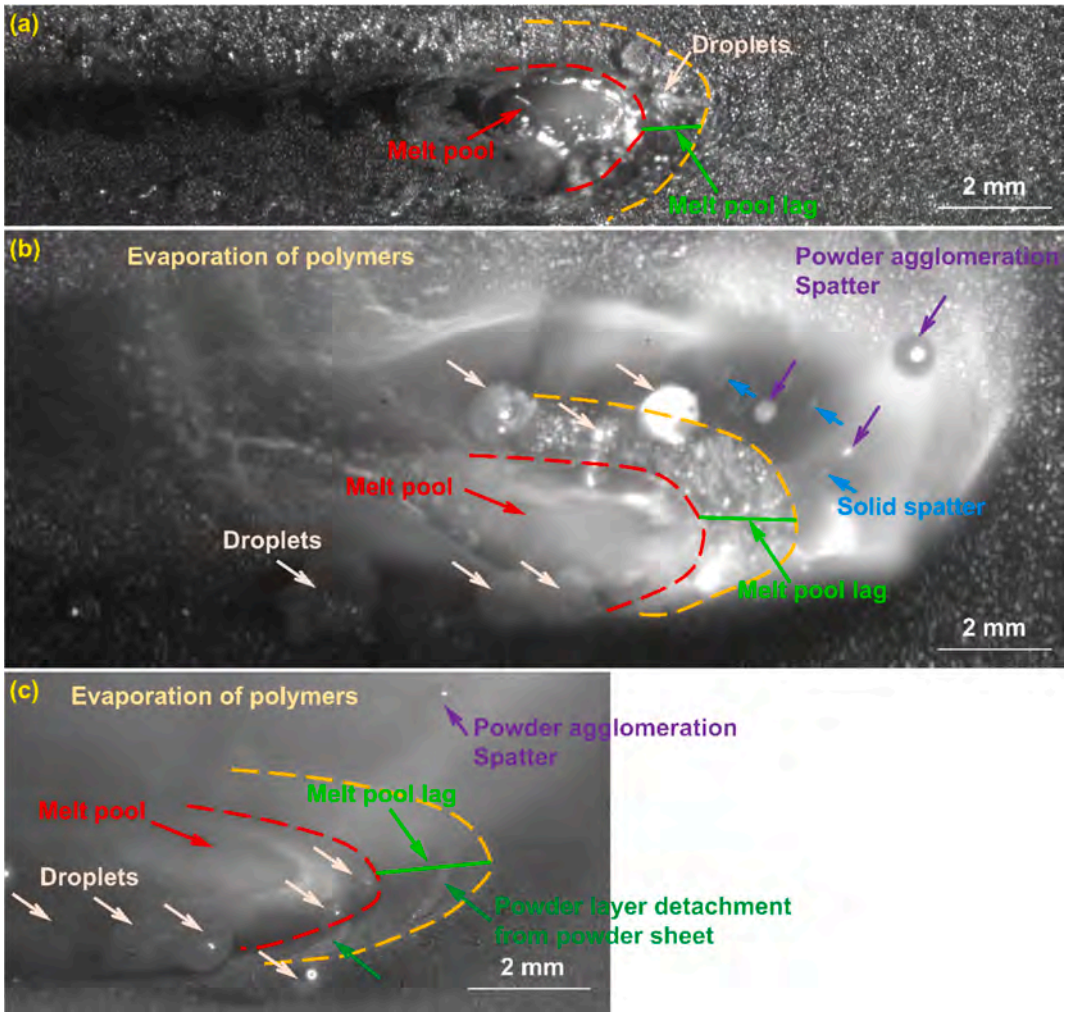

Fig. 6. High-speed imaging (HSI) frames of melt pool using powders and powder sheets (corresponding to Fig. 5). (a) HSI frame in Experiment No. 1 ($\Delta f = +30$ mm, 4.4 kW, 2 m/min, and powder); (b) HSI frame in No. 2 ($\Delta f = +30$ mm, 4.4 kW, 2 m/min, Type 0 powder sheet, and binder side up); (c) HSI frame in No. 3 ($\Delta f = +30$ mm, 4.4 kW, 1.5 m/min, Type 1 powder sheet, and powder side up).

section (shown in the insert view). However, when the powder side was up, there were even more inclusions with a smaller size in the cross section, and pores occurred (shown in Fig. 7b). In addition, the binder side up induced a narrow and deep melt pool while the powder side up orientation led to a wide and shallow melt pool, due to the fact that the binder side has a significant shielding effect on the laser energy transfer by the evaporation of the binder.

Fig. 8 shows the HSI frames of melt pool in Experiment Nos. 4 and 5 (corresponding to Fig. 7) and the illustrations of the melt pool dynamics. Fig. 8a-1 exhibits the HSI frame of the melt pool in Experimental No. 4 ($\Delta f = 0$, 3 kW, 2.4 m/min, Type 1 powder sheet and binder side up). It can be seen that the powder agglomeration spatter is occurring. The powders in the powder sheet consolidated after being fused and partly flew away due to the gas flow induced by the laser recoil pressure, illustrated in Fig. 8a-1 based on the High-Speed Video 4 in the supplementary materials. However, the phenomenon of solid spatter occurs when the powder side is up, accompanied by slight powder agglomeration spatter (Fig. 8b-1). Based on High-Speed Video 5 in the

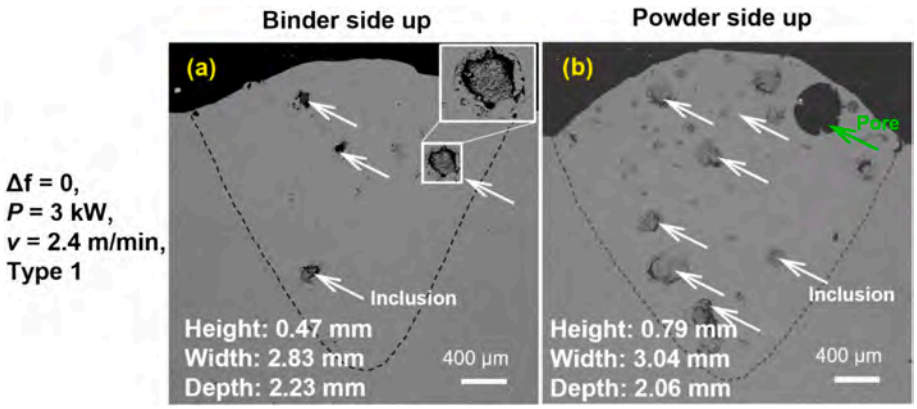

Fig. 7. Cross-section morphologies of the MAPS-tracks using Type 1 powder sheet when binder or powder side is up. (a) Experiment No. 4 (Δf = 0, 3 kW, 2.4 m/min, Type 1 powder sheet, and binder side up); (b) No. 5 (Δf = 0, 3 kW, 2.4 m/min, Type 1 powder sheet, and powder side up).

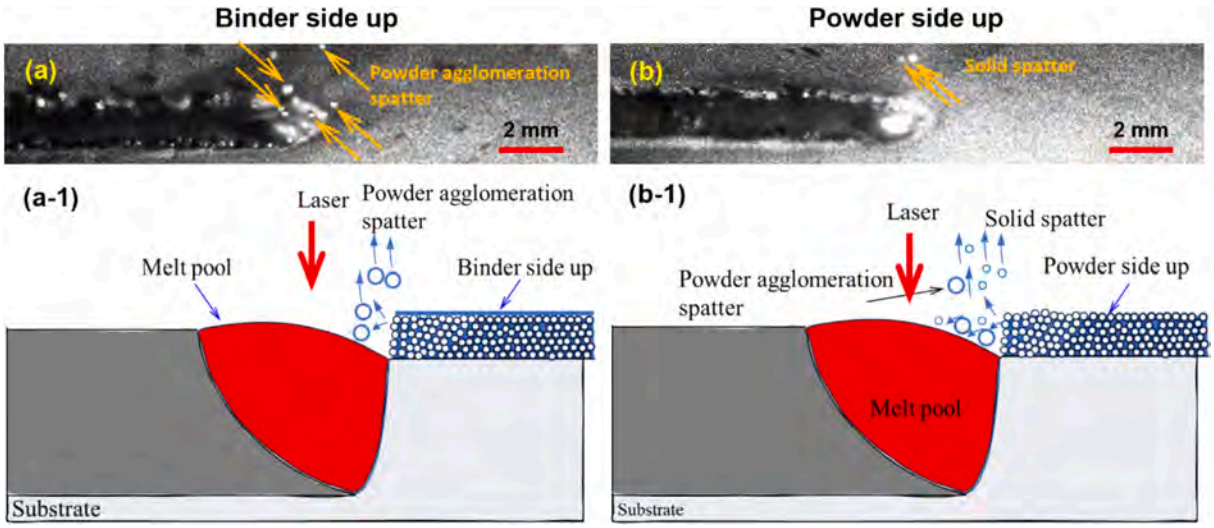

Fig. 8. High-speed imaging (HSI) frames of melt pool when binder or powder side is up (corresponding to Fig. 7) and the illustrations of the melt pool dynamics. (a) HSI frame and (a-1) the illustration in Experiment No. 4 (Δf = 0, 3 kW, 2.4 m/min, Type 1 powder sheet, binder side up); (b) HSI frame and (b-1) the illustration in No. 5 (Δf = 0, 3 kW, 2.4 m/min, Type 1 powder sheet, powder side up).

supplementary materials, the formation process of the spatter is shown in Fig. 8b-1. Binder side up, leading to more powder agglomeration spatter than powder side up (Fig. 8a and b), has taken more laser energy away, which is confirmed by the narrow and deep melt pool when binder side is up (Fig. 7a and b). In addition, there are no balling phenomena when binder side is up or powder side is down.

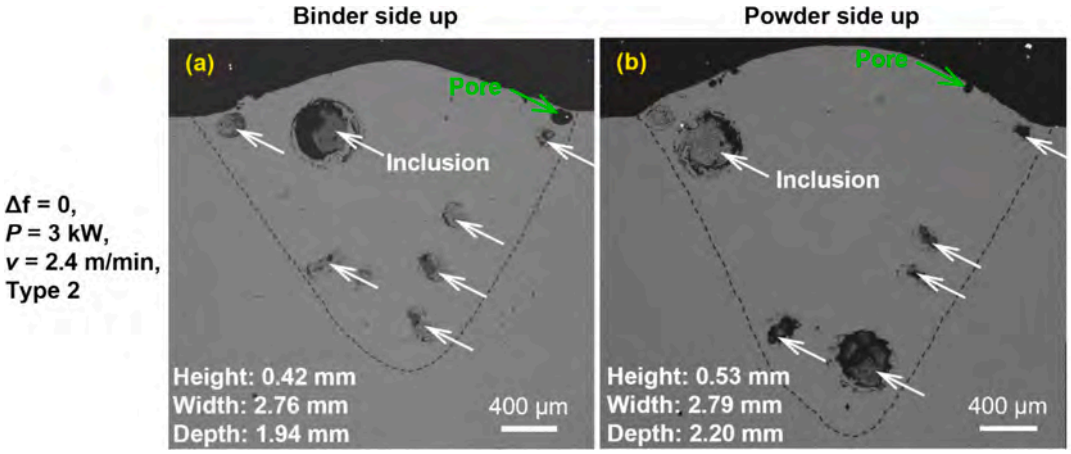

Fig. 9. Cross-section morphologies of the MAPS-tracks using Type 2 powder sheet when binder or powder side is up. (a) Experiment No. 7 (Δf = 0, 3 kW, 2.4 m/min, Type 2 powder sheet and binder side up); (b) No. 8 (Δf = 0, 3 kW, 2.4 m/min, Type 2 powder sheet, and powder side up).

Fig. 9 displays the cross-section morphologies of the MAPS-tracks using Type 2 powder sheet when binder or powder side is up (corresponding to Experiment Nos. 4 and 5 with parameters of $\Delta f = 0$ and 3 kW). It can be seen that the main defect is inclusions. A few small pores occurred close to the surface. Similarly, inclusions were observed in the cross section while the powder side is up in Fig. 9b, but the melt pool becomes larger than that when the binder side was up, since the shielding effect of the binder side on the laser energy transfer induces the small melt pool.

Fig. 10 displays the HSI frames of melt pool in Experiment Nos. 4 and 5 (corresponding to Fig. 9). When the scanning speed is 2.4 m/min, the binder side up leads to powder agglomeration spatter (Fig. 10a) while the powder side up induces both solid spatter and powder agglomeration spatter (Fig. 10b), which is similar to MAPS with Type 2 powder sheet. However, there is no balling phenomenon. Fig. 10a and b are obtained from High-Speed Videos 6 and 7 in the Supplementary Materials, respectively.

3.3. Defect and melt pool dynamics using different powder-sizes

Fig. 11 presents the cross-section morphologies of the MAPS-tracks using Type 1 and Type 2 powder sheets (corresponding to Experiment Nos. 4 and 7). It can be seen that Type 1 powder sheet leads to a larger melt pool width and depth (in Fig. 11a) than Type 2 powder sheet (in Fig. 11b). This is because the smaller powder particle in Type 1 (0–30 μm) compared to Type 2 (63–200 μm) need less laser energy to be melted due to the high surface energy of smaller powders and thus more energy of the laser beam is used to generate the melt pool in the substrate. Type 1 powder sheet induced smaller inclusions than Type 2 powder sheet, because the small particles easily induced a smaller droplet than the large particles, and thus the polymers covered on the small droplets' surfaces will form small inclusions.

3.4. Defect and melt pool dynamics at different defocusing

Fig. 12 shows the cross-section morphologies of the MAPS-tracks and the corresponding melt pool dynamics at different defocusing (corresponding to Experiment Nos. 3 and 7). Fig. 12a presents the cross-section morphology of the MAPS-track when $\Delta f = 0$. The cross-section morphology is bell-shaped and there are inclusions at the bottom of the melt pool. The corresponding melt pool dynamics exhibited in Fig. 12a-1 (corresponding to High-Speed Video 8 in Supplementary Materials), shows that the balling phenomenon occurred accompanied by powder agglomeration spatter. There is no melt pool lag. When the defocusing increases to + 30 mm, the cross-section morphology shows that the size of the melt pool decreases significantly (shown in Fig. 12b) due to the conduction mode laser melting, and there are no inclusions and pores, suggesting that no material was added. The corresponding melt pool feature shown in Fig. 12b-1 (corresponding to High-Speed Video 9 in Supplementary Materials), shows that the powder sheet has melted and presented the balling phenomenon along the two sides of the track. In addition, there is a melt pool lag occurring between the melt pool and powder sheet.

3.5. Defect and melt pool dynamics with different scanning speeds

Fig. 13 shows the cross-section morphologies of the MAPS tracks and the corresponding high-speed images during the MAPS-AlSi10Mg process with different scanning speeds (corresponding to Experimental Nos. 4 and 6). Fig. 13a exhibits the cross-section morphology of the MAPS track when the scanning speed is 2.4 m/min. There are some inclusions within the track, but less at a low scanning speed of 1.5 m/min (shown in Fig. 13b). In addition, the height of the melt pool with low scanning speed decreases, suggesting that less droplets are captured by the melt pool. This is consistent with the phenomenon that fewer inclusions with a low scanning speed. From the high-speed imaging frames in Fig. 13a-1 (High-Speed Video 4) and b-1 (High-Speed Video 8), the powder agglomeration spatter phenomena appeared, but the low scanning speed induces balling, indicating that less material was added.

With Type 2 powder sheet powder sheet, the melt pool size becomes large with the low scanning speed (Fig. 14a and b). More and larger pores were generated in this case, due to the shielding gas/binder vapor was wrapped into the melt pool. There was no balling observed in both cases, but powder agglomeration spatter occurred shown in Fig. 14a-1 (shown in High-Speed Video 6 of Supplementary Materials) and b-1 (presented in High-Speed Video 10 of Supplementary Materials).

3.6. Defect and melt pool dynamics at different average laser intensities

Fig. 15 shows the cross-section morphologies of the MAPS-tracks and the corresponding high-speed imaging frames during the MAPS-AlSi10Mg (Type 1 powder sheet) process at different average laser intensities (corresponding to Experiment Nos. 11 and 12). Fig. 15a presents the cross-section morphologies of the tracks with the average laser intensity of 1.1×10^5 W/cm^2. It can be seen some inclusions occurred in the track. However, when the average laser intensity increased to 1.6×10^5 W/cm^2, the inclusions almost disappeared (Fig. 15b). It is worth mentioning that there are few small inclusions within the track,

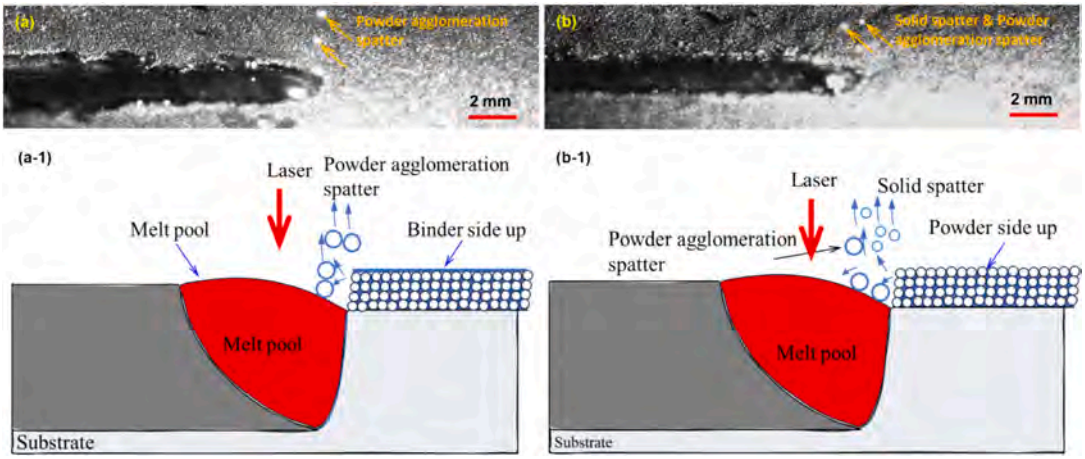

Fig. 10. High-speed imaging (HSI) frames of melt pool when binder or powder side is up (corresponding to Fig. 9). (a) HSI frame and (a-1) the illustration in Experiment No. 7 ($\Delta f = 0$, 3 kW, 2.4 m/min, Type 2 powder sheet, binder side up); (b) HSI frame and (b-1) the illustration in No. 8 ($\Delta f = 0$, 3 kW, 2.4 m/min, Type 2 powder sheet, powder side up).

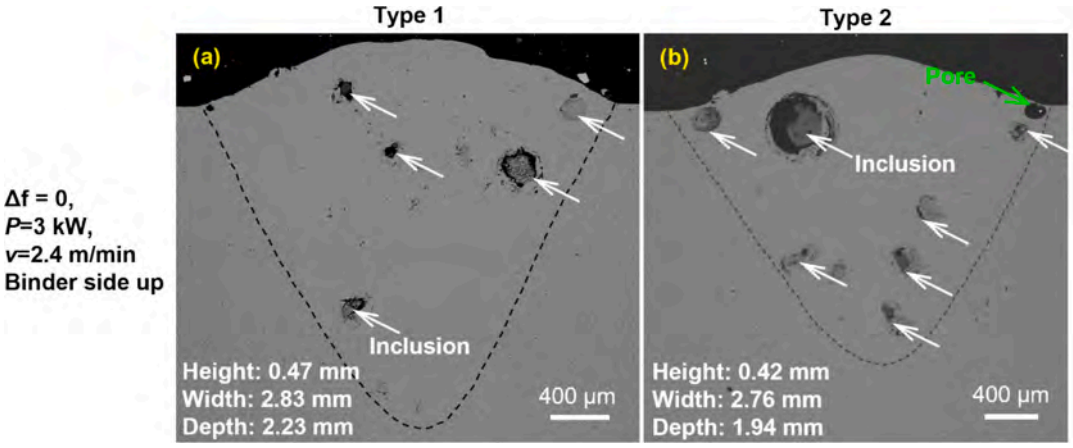

Fig. 11. Cross-section morphologies of the MAPS-tracks using Type 1 and Type 2 powder sheets. (a) Experiment No. 4 ($\Delta f = 0$, 3 kW, 2.4 m/min, Type 1, binder side up); (b) No. 7 ($\Delta f = 0$, 3 kW, 2.4 m/min, Type 2, and binder side up).

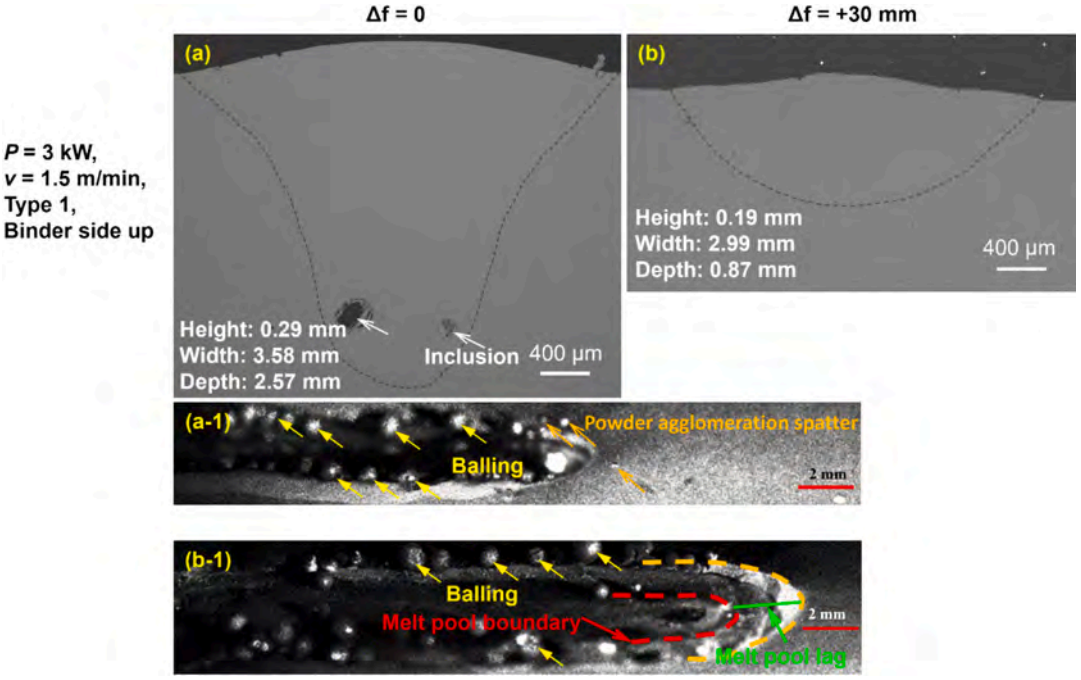

Fig. 12. Cross-section morphologies of the MAPS tracks and the corresponding high-speed images using different defocusing of 0 and + 30 mm. (a) Experiment No. 6 ($\Delta f = 0$, 3 kW, 1.5 m/min, Type 1 powder sheet, binder side up) and (a-1) the corresponding high-speed imaging frame; (b) No. 10 ($\Delta f = +30mm$, 3 kW, 1.5 m/min, Type 1 powder sheet, binder side up) and (b-1) the corresponding high-speed imaging frame.

suggesting the defects have been basically suppressed. The corresponding high-speed imaging frames in Fig. 15a-1 (exhibited in High-Speed Video 11 of Supplementary Materials) and b-1 (shown in High-Speed Video 12 of Supplementary Materials) both present a balling, suggesting that the powder sheet has locally melted to form droplets and part of them were distributed around the two boundaries of the track. Furthermore, in the melt pool lag areas, the interaction between the laser and the powder sheet is more intense than at low average laser intensity. For a higher average laser intensity (Fig. 15b-1), the polymer binder can evaporate or be taken away by the powder agglomeration spatter more effectively. Thus, there are less inclusions within the tracks (Fig. 15b).

4. Discussion

4.1. Mass transfer during MAPS process

From the HSI frames in Fig. 6, there is a big difference in melt pool dynamics between preplaced-powder additive manufacturing and MAPS regarding spatter phenomenon, balling phenomenon, and polymer evaporation, which significantly affect the mass transfer. To fully understand the mass transfer during MAPS process, the melt pool dynamics during preplaced-powder additive manufacturing process were firstly illustrated based on Fig. 6a and the high-speed videos in Ref. [20], as shown in Fig. 16. With a much defocusing or low scanning speed, the melt pool lag area generates, which makes the powders flow towards the melt pool, illustrated in Fig. 16a. In the melt pool lag area, some of the powders are melted into droplets and finally the powders or generated droplets are incorporated into the melt pool. Note that some un-

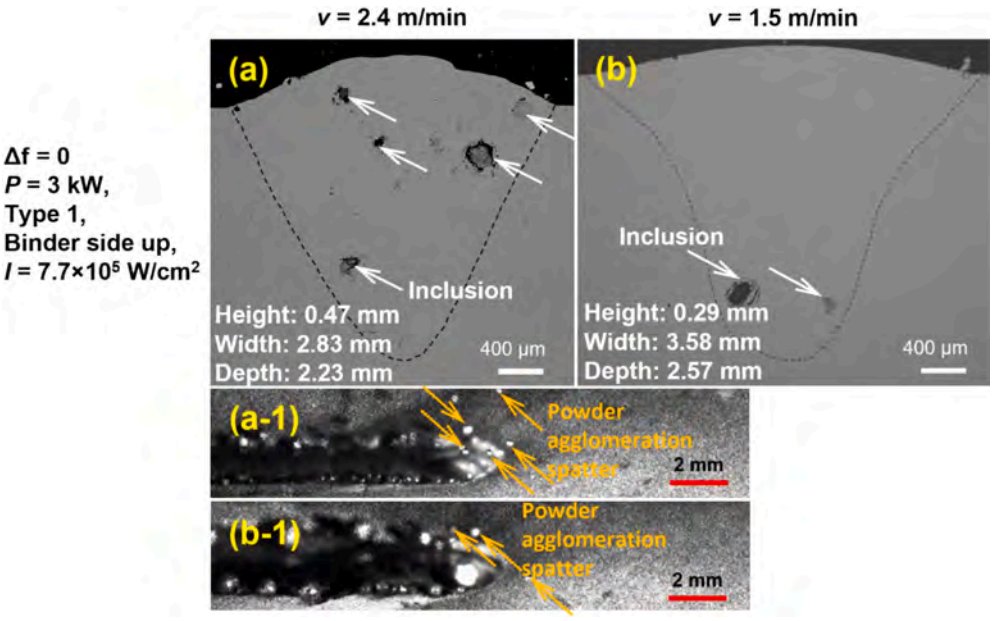

Fig. 13. Cross-section morphologies of the MAPS-tracks and the corresponding high-speed images during the MAPS-AlSi10Mg (Type 1 powder sheet) process with different scanning speeds of 2.4 and 1.5 m/min. (a) Experiment No. 4 ($\Delta f = 0$, 3 kW, 2.4 m/min, Type 1 powder sheet, binder side up and $I = 7.7 \times 10^5$ W/cm^2) and (a-1) the corresponding high-speed imaging frame; (b) No. 6 ($\Delta f = 0$, 3 kW, 1.5 m/min, Type 1 powder sheet, binder side up and $I = 7.7 \times 10^5$ W/cm^2) and (b-1) the corresponding high-speed imaging frame.

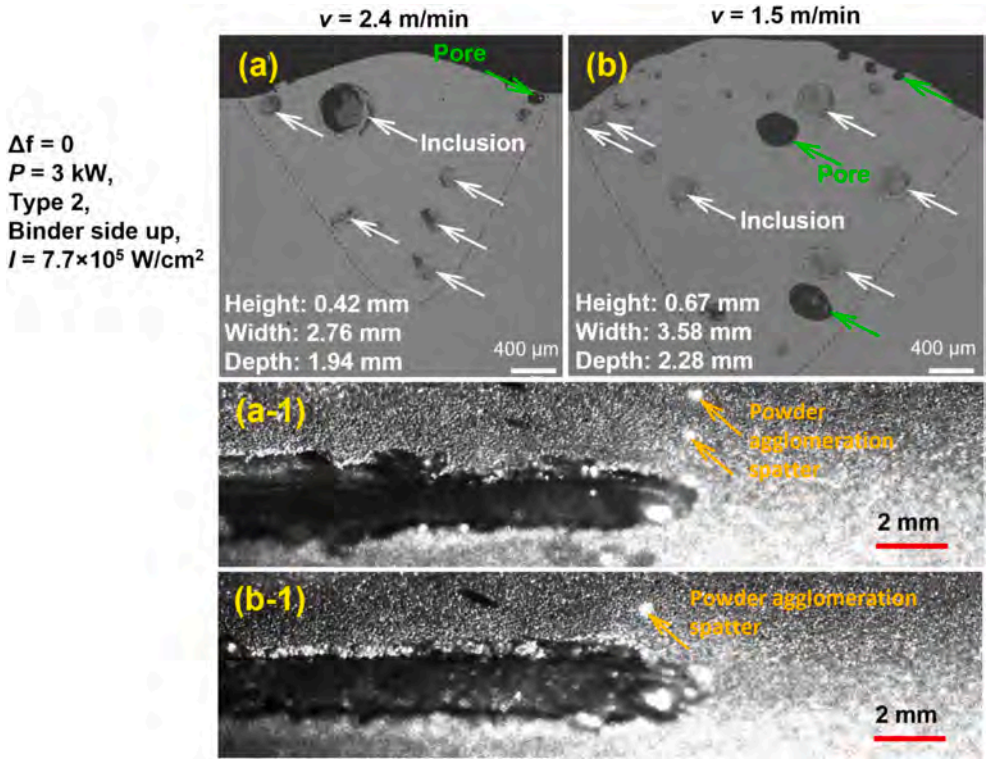

Fig. 14. Cross-section morphologies of the MAPS-tracks and the corresponding high-speed images during the MAPS-AlSi10Mg (Type 2 powder sheet) process with different scanning speeds of 2.4 and 1.5 m/min. (a) Experiment No. 7 ($\Delta f = 0$, 3 kW, 2.4 m/min, Type 2 powder sheet, binder side up and $I = 7.7 \times 10^5$ W/cm^2) and (a-1) the corresponding high-speed imaging frame; (b) No. 9 ($\Delta f = 0$, 3 kW, 1.5 m/min, Type 2 powder sheet, binder side up and $I = 7.7 \times 10^5$ W/cm^2) and (b-1) the corresponding high-speed imaging frame.

incorporated droplets are survived along the two sides of the track. Using a small defocusing or medium scanning speed (Fig. 16b), the melt pool lag area becomes smaller and some powders and droplets within this area are incorporated into the melt pool. Meanwhile, the solid spatter becomes severe due to the gas flow induced by the recoil pressure. Employing a focused laser or high scanning speed (Fig. 16c), the melt pool lag area disappears while the intense solid spatter occurs.

For MAPS-AlSi10Mg process, the HSI frames (Figs. 6b,c, 8, and

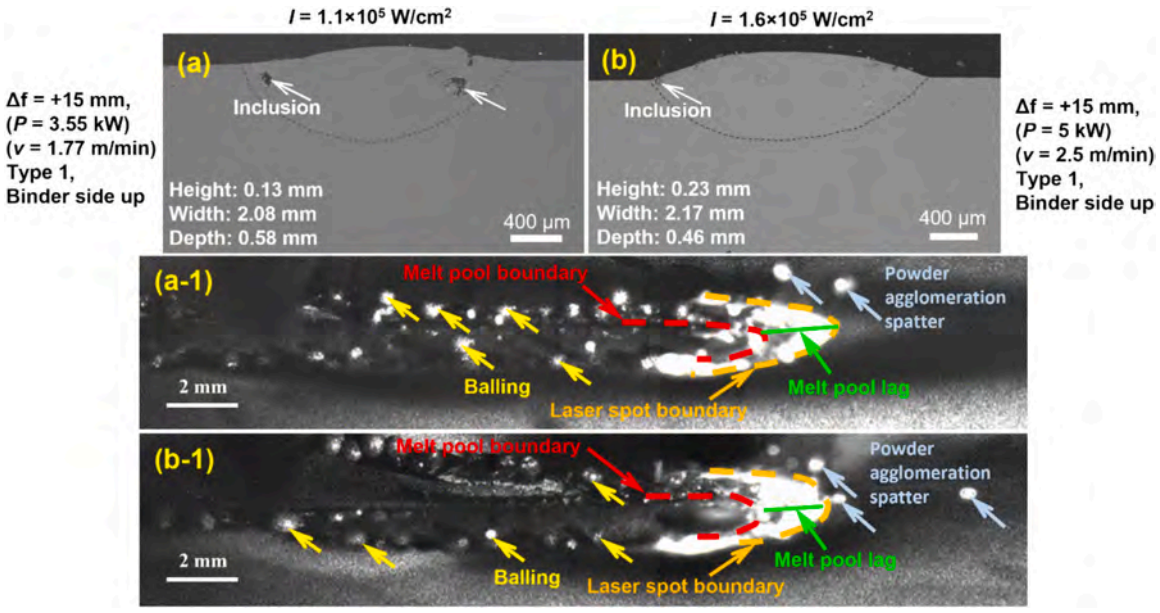

Fig. 15. Cross-section morphologies of the MAPS-tracks and the corresponding high-speed images during the MAPS-AlSi10Mg (Type 1 powder sheet) process with different average laser intensities of 1.1×10^5 and 1.6×10^5 W/cm^2. (a) Experiment No. 11 ($\Delta f = +15$ mm, 3.55 kW, 1.77 m/min, Type 1 powder sheet, binder side up and $I = 1.1 \times 10^5$ W/cm^2) and (a-1) the corresponding high-speed imaging frame; (b) No. 12 ($\Delta f = +15$ mm, 5 kW, 2.5 m/min, Type 1 powder sheet, binder side up and $I = 1.6 \times 10^5$ W/cm^2) and (b-1) the corresponding high-speed imaging frame.

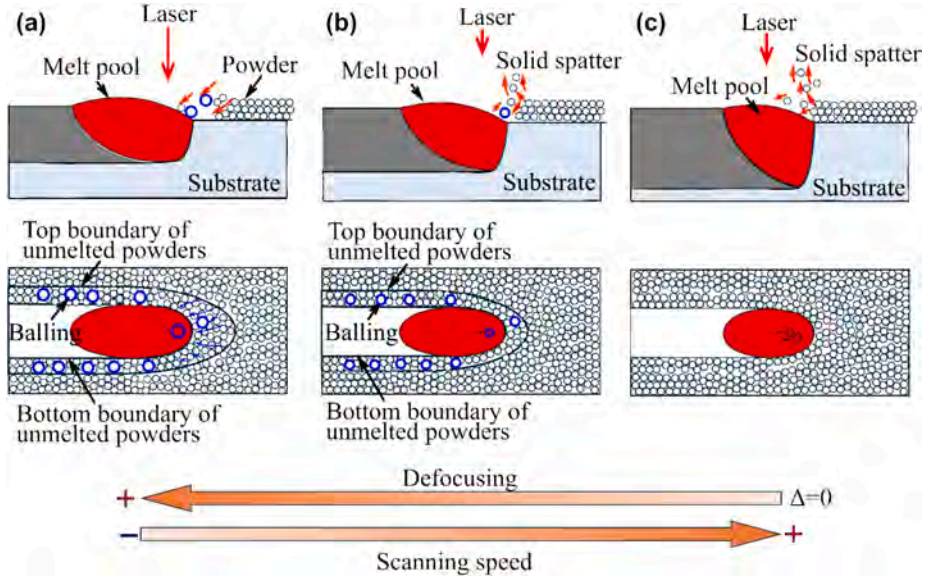

Fig. 16. Illustrations of materials mass transfer during preplaced-powder additive manufacturing process with the decreasing defocusing or increasing scanning speed. (a) With a much defocusing or low scanning speed, (b) a small defocusing or medium scanning speed, and (c) a focused laser beam or high scanning speed.

10–13) show that the parameters related to powder sheet (binder/powder side up, powder particle size) and laser (defocusing, scanning speed, average laser intensity) influence the mass transfer process. For instance, binder side up conditions can realize the mass transfer process only via large droplets being captured by the melt pool while powder side up arrangements via both small and large droplets being captured with focused laser and small particle-size (0–30 μm) powder sheet. Powder sheet with larger particle-size distributions (60–200 μm) and small defocusing both promote the droplets being captured. Obviously, the processing parameters which influence the interactions between the laser and the powder sheet in front of the melt pool control the mass transfer process.

Fig. 17 illustrates the mass transfer process at different defocusing when the binder side of the small particle-size powder sheet is up. With a much defocusing (shown in the front view of Fig. 14a), there is a big gap between the melt pool front and powder sheet, which is called melt pool lag. In this case, the surface powder layer absorbing laser was detached from powder sheet. At the same time, the wrapped powder layer will melt and gather to form a droplet, moving along the two sides of the track. Finally, the balling phenomenon occurs shown in the top view and no droplets are captured by the melt pool. When the defocusing decreases (shown in the front view of Fig. 17b), the wrapped powder layer disappears and the droplets form directly on the surface. As a result, some of the uncaptured droplets induce balling, while some form spatter flying away with the help of the impact of the laser recoil pressure and others move into the melt pool. Note that this kind of defocusing can

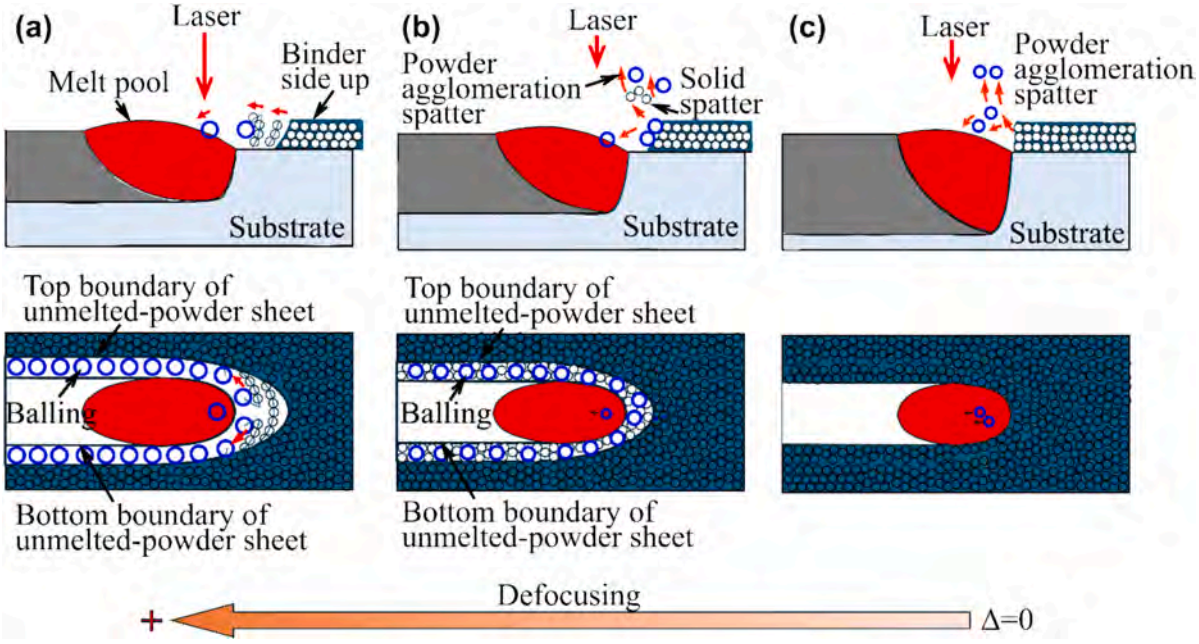

Fig. 17. Illustrations of materials mass transfer during MAPS process at different defocusing when binder side is up. (a) With a much defocusing (b) a small defocusing, and (c) a focused laser beam.

make the droplets formed in the melt pool lag and the polymers have enough time to evaporate from the powder sheet, which can lead to defect-free tracks (as shown in Fig. 15b). When the defocusing decreases to 0 (in Fig. 17c), there is no melt pool lag and powder agglomeration spatter occur. Some droplets move towards the melt pool. When the scanning speed is too low or too high, the balling phenomenon or solid spatter become more serious for all the defocusing, which decrease the mass transfer process.

Fig. 18 illustrates the mass transfer process at different defocusing when the powder side of small particle-size powder sheet is up. When the defocusing is much (shown in Fig. 18a), the powder layer in the melt pool lag area detaches from the powder sheet, melts into droplet and moves along the tracks to induce balling phenomenon finally. With the decreasing of defocusing, the smaller droplets formed. Some of them move along both sides of the track, some of them are captured by the melt pool, and others form powder agglomeration spatter. When using a focused laser beam, there is no melt pool lag, but some of the powder particles and droplets are captured by the melt pool. A low or high scanning speed induces balling phenomenon.

Except spatters, there is no obvious difference between particle-size distributions of the powder in the sheet and mass transfer process. Their mass transfer processes are realized both via droplets formed from the powder sheet in front of the melt pool and incorporation of the droplet into the melt pool. However, the large particle-size distributions of the powder in the sheet induces a small melt pool since the smaller powders possess higher surface energy than that of the large powders and thus it need less laser energy to melt the smaller powders and more energy is used to generate the melt pool in the substrate. For a high scanning speed, it leads to a smaller melt pool with balling and thus reduces the mass transfer. In addition, there is also no evident relation between average laser intensity and mass transfer.

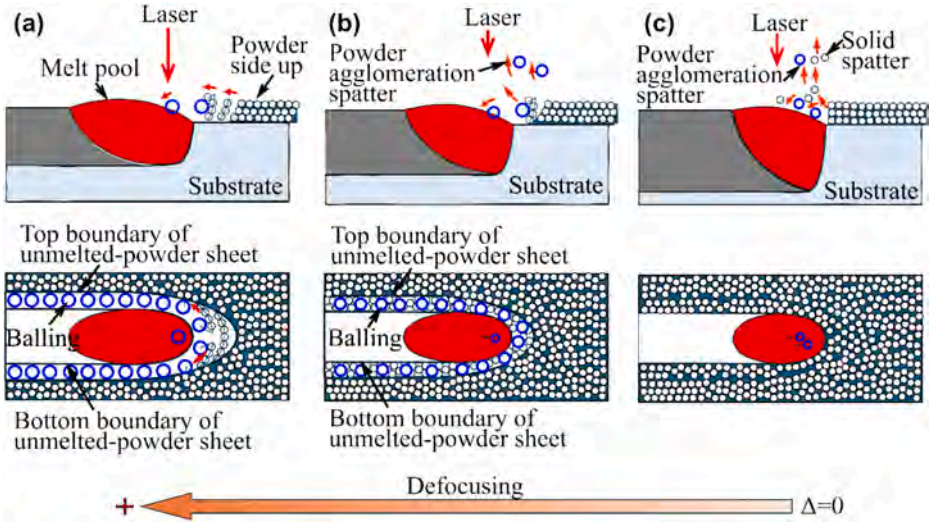

Fig. 18. Illustrations of materials mass transfer during MAPS process with different defocusing when powder side is up. (a) With a much defocusing, (b) a small defocusing, and (c) a focused laser beam.

4.2. Defect formation during MAPS process

There were no defects identified in the powder tracks with preplaced powder (Fig. 5a), but defects occurred in the MAPS-tracks (Fig. 5b and c), suggesting it is the powder sheet that induces the formation of defects. Seen from the cross-section morphologies of the tracks (Figs. 5, 7, 9–13), the main defects comprise inclusions and pores. Among them, the inclusions are commonly observed. The circular morphology of the inclusions suggests that these inclusions come from the droplets captured by melt pool. Although the temperature of the melt pool is high (more than 600 ℃), the position where sheets melt in front of the melt pool is far away from this temperature, which promotes the incomplete evaporation of polymers. From the videos, during the formation of droplets, the unevaporated polymers (bright color in the Videos 2 and 3) were covered on the droplets' surfaces or directly wrapped into the droplets.

Fig. 19 shows the morphologies of the inclusions. The inclusions present black circle profiles, suggesting that the surfaces of droplets are covered by polymers. This polymer layer possibly comes from the unevaporated polymers or the attachment of polymer vapor. The evaporation of polymer occurs around the melt pool and the formed droplets can be polluted by the vapor. Inside the droplets, some black "coatings" can be seen. At the beginning of the interactions between laser and powder sheet with a focused laser beam, the melting of the powders and the melting/evaporation of polymers occurred simultaneously, and thus the liquid aluminum alloy and liquid polymers (even polymer vapor) mixed to form the droplets with inclusions.

When the defocusing of $\Delta f = +15$ mm was employed, a track without defects was obtained (Fig. 15b). In this situation, there is a melt pool lag area where the polymer within the powder sheet has enough energy and time to evaporate. The powder agglomeration spatter also took away some polymers. Therefore, there are no polymers left in the tracks. This provides a way to obtain defect-free tracks. Furthermore, when the scanning speed is low enough, some pores were included into the melt pool due to the strong laser recoil pressure induces more shielding gas or binder vapor incorporated into the intensive boiling melt pool.

5. Conclusions

This work systematically investigated the mass transfer and defect formation during metal additive manufacturing using power sheet-AlSi10Mg (MAPS-AlSi10Mg) by changing the processing parameters regarding powder sheet (orientation, powder particle size) and laser directed energy deposition (defocusing, scanning speed, average laser intensity). The cross-sections of the tracks were observed to study the defects, and the high-speed imaging frames were employed to characterize and analyze the melt pool dynamics. The conclusions can be summarized as follows.

(1) The mass transfer of MAPS-AlSi10Mg was realized via droplets formed in front of the melt pool and incorporation of the droplet into the melt pool. The polymer within the powder sheet directly induced the defect formation of inclusions and pores by incomplete evaporation of polymers and shielding gas/binder vapor involvement.
(2) Binder side up induces less droplets being captured by the melt pool than powder side up with a focused laser due to more powder agglomeration spatter when binder side is up. Furthermore, the powder side up induces a wider melt pool than binder side up since the evaporation of polymers when binder side is up consumes more laser energy.
(3) Large powder-particle powder sheets promote a higher deposition rate than small powder-particle powder sheets during MAPS by forming larger and heavier droplets and more easily being incorporated into the melt pool.
(4) Melt pool lag determined by laser defocusing, makes a difference in mass transfer and defect formation. A large melt pool induces more balling and limits the droplets incorporation into the melt pool. However, a suitable melt pool lag generates inclusion-free tracks by leading to the sufficient evaporation of polymers and the powder agglomeration spatters to completely remove the polymers.

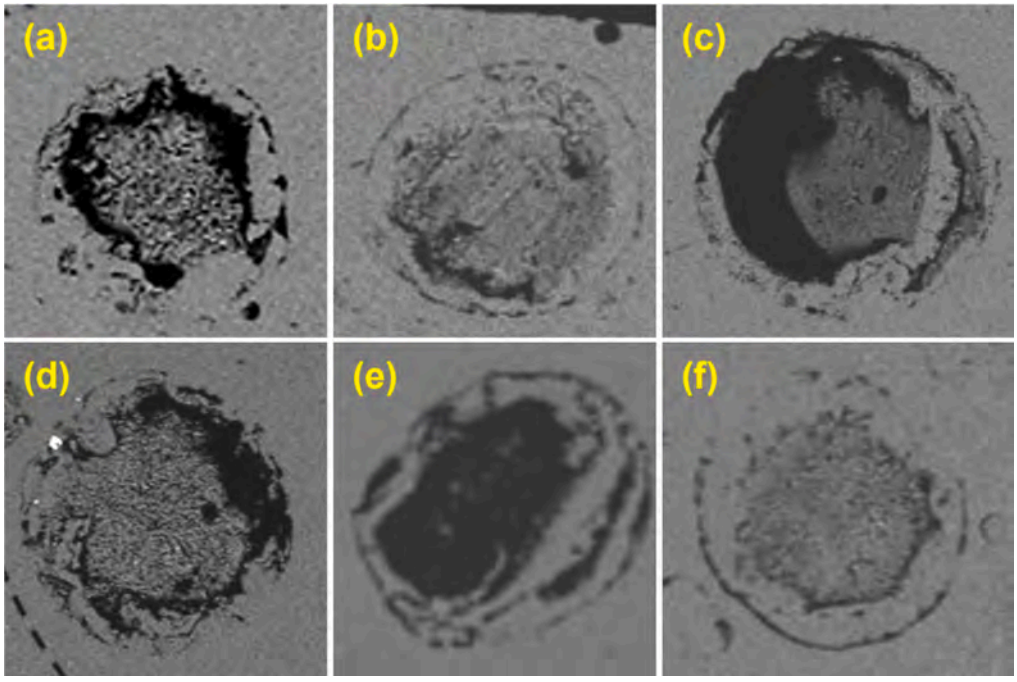

Fig. 19. Morphologies of inclusions within the tracks in different experiments. (a) Experiment No. 4 ($\Delta f = 0$, 3 kW, 2.4 m/min, Type 1 powder sheet, and binder side up); (b) No. 5 ($\Delta f = 0$, 3 kW, 2.4 m/min, Type 1 powder sheet, and powder side up); (c) No. 7 ($\Delta f = 0$, 3 kW, 2.4 m/min, Type 2 powder sheet and binder side up); (d) No. 8 ($\Delta f = 0$, 3 kW, 2.4 m/min, Type 2 powder sheet, and powder side up); (e) No. 6 ($\Delta f = 0$, 3 kW, 1.5 m/min, Type 1, binder side up); (f) No. 9 ($\Delta f = 0$, 3 kW, 1.5 m/min, Type 2, and binder side up).

(5) The MAPS process offers the possibility to build and repair complex parts among others for lightweight e-mobility applications.

Improvements to the MAPS process, including reducing powder agglomeration spatter and promoting the evaporation of the polymer, would result in higher deposition-efficiency MAPS process without defects. For large-scale components fabricated by MAPS, how to set the overlap ratio and how to distribute the powder sheet around the overlapped area based on the DED-LB/M setup still need to investigate deeply. Moreover, for a MAPS-parts with small amount of inclusions defect or high-level carbon, the post-processing of removing the defects and decrease carbon is important research orientation.

CRediT authorship contribution statement

Pengfei Guo: Writing – original draft, Investigation, Data curation, Validation, Formal analysis, Methodology, Conceptualization. **Joerg Volpp:** Writing – review & editing, Formal analysis, Investigation, Conceptualization, Methodology, Funding acquisition. **Himani Naesstroem:** Writing – review & editing, Investigation, Methodology, Formal analysis. **Silvia Marola:** Investigation, Formal analysis. **Wenyou Zhang:** Investigation, Methodology, Conceptualization. **Johanne Mouzon:** Formal analysis, Investigation. **Riccardo Casati:** Investigation, Data curation. **Michael Gibbons:** Methodology, Supervision. **Rocco Lupoi:** Methodology, Resources, Formal analysis, Funding acquisition. **Alexander F.H. Kaplan:** Resources, Supervision, Writing – review & editing, Project administration.

Declaration of competing interest

The authors declare that they have no known competing financial interests or personal relationships that could have appeared to influence the work reported in this paper.

Acknowledgements

This work was supported by PosAddive – Powder Sheet Additive Manufacturing (EIT RawMaterials, Proposal No. 22021) and SMART – Surface tension of Metals Above vapoRization Temperature (Vetenskapsrådet - The Swedish Research Council, 2020-04250). We thank Tore Silver and Roger Engman for the technical supports during the MAPS-AlSi10Mg experiments. We also acknowledge Asli Coban, Maria Ellinor Holmstroem and Moyin Otubela for the useful discussion.

Appendix A. Supplementary data

Supplementary data to this article can be found online at https://doi.org/10.1016/j.optlastec.2025.113495.

References

[1] A. Parthasarathy, Flying cars-Next stop for urban e-mobility, Science Reporter, National Institute of Science Communication and Policy Research (NIScPR), Council of Scientific and Industrial Research (CSIR), New Delhi, 2022, pp. 15-19. http://nopr.niscpr.res.in/handle/123456789/60625.

[2] A. Mahr, T. Schütt, T. Rosnitschek, S. Tremmel, F. Döpper, Evaluation of Powder- and Extrusion-based Metal Additive Manufacturing Processes for the Sustainable Fabrication of Spare Parts in Electromobility, Sustainability 16 (2024) 3425, https://doi.org/10.3390/su16083425.

[3] M.A.S. Linnenbrink, N. Pirch, A. Gasser, H. Schleifenbaum, DED for repair and manufacture of turbomachinery components, in: A.T.V. Esposito (Ed.), 3D Printing for Energy Applications, The American Ceramic Society, 2021, pp. 307–326.

[4] D. Gu, X. Shi, R. Poprawe, D.L. Bourell, R. Setchi, J. Zhu, Material-structure-performance integrated laser-metal additive manufacturing, Science 372 (2021) eabg1487, https://doi.org/10.1126/science.abg1487.

[5] Z. Li, S. Sui, X. Ma, H. Tan, C. Zhong, G. Bi, A.T. Clare, A. Gasser, J. Chen, High deposition rate powder- and wire-based laser directed energy deposition of metallic materials: a review, Int J Mach Tool Manu 181 (2022) 103942, https://doi.org/10.1016/j.ijmachtools.2022.103942.

[6] H. Lv, Y. Liu, H. Chen, W. Zhang, S. Lv, D. He, Temperature field simulation and microstructure evolution of Fe-based coating processed by extreme high-speed laser cladding for re-manufacturing locomotive axle, Surf. Coat. Technol. 464 (2023) 129529, https://doi.org/10.1016/j.surfcoat.2023.129529.

[7] S. Sui, J. Chen, L. Ma, W. Fan, H. Tan, F. Liu, X. Lin, Microstructures and stress rupture properties of pulse laser repaired Inconel 718 superalloy after different heat treatments, J. Alloy. Compd. 770 (2019) 125–135, https://doi.org/10.1016/j.jallcom.2018.08.063.

[8] A. Saboori, A. Aversa, G. Marchese, S. Biamino, M. Lombardi, P. Fino, Application of Directed Energy Deposition-based Additive Manufacturing in Repair, Appl. Sci. 9 (2019) 3316, https://doi.org/10.3390/app9163316.

[9] Q. Wu, W. Long, L. Zhang, H. Zhao, A review on ceramic coatings prepared by laser cladding technology, Opt. Laser Technol. 176 (2024) 110993, https://doi.org/10.1016/j.optlastec.2024.110993.

[10] D. Svetlizky, M. Das, B. Zheng, A.L. Vyatskikh, S. Bose, A. Bandyopadhyay, J. M. Schoenung, E.J. Lavernia, N. Eliaz, Directed energy deposition (DED) additive manufacturing: Physical characteristics, defects, challenges and applications, Mater. Today 49 (2021) 271–295, https://doi.org/10.1016/j.mattod.2021.03.020.

[11] D. Koti, J. Powell, H. Naesstroem, K.T. Voisey, Powder catchment efficiency in laser cladding (directed energy deposition). an investigation into standard laser cladding and the ABA cladding technique, J. Laser Appl. 35 (2023) 012025, https://doi.org/10.2351/7.0000904.

[12] R. Lupoi, W.M. Abbott, R. Senthamaraikannan, S. McConnell, J. Connolly, S. Yin, R.B. Padamati, Metal additive manufacturing via a novel composite material using powder and polymers formed in sheets, CIRP Ann.-Manuf. Technol. 71 (2022) 181–184, https://doi.org/10.1016/j.cirp.2022.03.012.

[13] W. Zhang, X. Lu, A. Coban, M. Cervera, M. Chiumenti, A. Sasnauskas, C. Huang, S. Yin, R.P. Babu, R. Lupoi, Powder sheet additive manufacturing of multi-material structures: Experimental and computational characterizations, Compos. Part B-Eng. 272 (2024) 111203, https://doi.org/10.1016/j.compositesb.2024.111203.

[14] W. Zhang, W.M. Abbott, A. Sasnauskas, A. Coban, B. Gillham, I. Bitharas, S. Lu, J. Quirke, S. Ruan, K. Perkins, K. Synnatschke, M. Moebius, S. Yin, A. Moore, R. P. Babu, R. Lupoi, Development of a novel powder sheets printing process towards the next generation of additive manufacturing: the role of laser defocusing, Virtual Phys. Prototyp. 19 (2024) e2361856, https://doi.org/10.1080/17452759.2024.2361856.

[15] W. Zhang, A. Coban, A. Sasnauskas, Z. Cai, B. Gillham, W. Mirihanage, S. Yin, R. P. Babu, R. Lupoi, A novel powder sheet laser additive manufacturing method using irregular morphology feedstock, CIRP J. Manuf. Sci. Technol. 52 (2024) 26–35, https://doi.org/10.1016/j.cirpj.2024.05.007.

[16] W. Zhang, S. Marola, S. McConnell, Z. Cai, J. Dugenio, M. Li, W.M. Abbott, A. Coban, A. Sasnauskas, S. Yin, R. Padamati Babu, W. Mirihanage, R. Casati, R. Lupoi, Demonstration and benchmarking of a novel powder sheet additive manufacturing approach with austenitic steel, Mater. Design. 245 (2024) 113301, https://doi.org/10.1016/j.matdes.2024.113301.

[17] A. Sasnauskas, A. Coban, W. Zhang, W.M. Abbot, R.P. Babu, M.-S. Pham, R. Lupoi, Metal additive manufacturing using powder sheets (MAPS) of HEA CoNiCrFeMn: the effect of the polymer content on microstructure and mechanical properties, CIRP Ann.-Manuf. Technol. 73 (2024) 173–176, https://doi.org/10.1016/j.cirp.2024.04.066.

[18] C. Tan, F. Weng, S. Sui, Y. Chew, G. Bi, Progress and perspectives in laser additive manufacturing of key aeroengine materials, Int J Mach Tool Manu 170 (2021) 103804, https://doi.org/10.1016/j.ijmachtools.2021.103804.

[19] Z.A. Young, Q. Guo, N.D. Parab, C. Zhao, M. Qu, L.I. Escano, K. Fezzaa, W. Everhart, T. Sun, L. Chen, Types of spatter and their features and formation mechanisms in laser powder bed fusion additive manufacturing process, Addit. Manuf. 36 (2020) 101438, https://doi.org/10.1016/j.addma.2020.101438.

[20] P. Bidare, I. Bitharas, R.M. Ward, M.M. Attallah, A.J. Moore, Fluid and particle dynamics in laser powder bed fusion, Acta Mater. 142 (2018) 107–120, https://doi.org/10.1016/j.actamat.2017.09.051.